ROYAL SOCIETY
OF CHEMISTRY

PAPER

Check for updates

3D printed strontium–zinc-phosphate bioceramic scaffolds with multiple biological functions for bone tissue regeneration†

Li Deng,‡[ab] Lingwei Huang, [iD] ‡[bcg] Hao Pan,‡[ce] Qi Zhang,[ce] Yumei Que,[bc] Chen Fan,[bc] Jiang Chang, [iD] *[bcf] Siyu Ni*[d] and Chen Yang [iD] *[abcd]

Calcium phosphate (CaP) bioceramics are broadly employed for bone regeneration due to their excellent biocompatibility and osteoconductivity. However, they are not capable of repairing healing-impaired bone defects such as defects with conditions of ischemia or infection due to restricted bioactivities. In this study, we synthesized single-phased strontium–zinc-phosphate (SZP, $SrZn_2(PO_4)_2$) bioceramics *via* a solution combustion method and further fabricated SZP scaffolds using a three-dimensional (3D) printing technique. Compared to 3D printed β-tricalcium phosphate (β-TCP) scaffolds, the 3D printed SZP scaffolds presented comparable porosity, compressive strength, and Young's modulus, but increased ability of osteogenesis, angiogenesis, immunomodulation and anti-bacterial activity. Specifically, 3D printed SZP scaffolds not only led to significantly higher osteogenic differentiation of MC3T3-E1 cells and pro-angiogenesis of human umbilical vein endothelial cells (HUVECs) directly or through macrophage-mediated immunomodulation, but also inhibited the growth of *Staphylococcus aureus* (*S. aureus*) and *Escherichia coli* (*E. coli*). The *in vivo* study of the rat cranial bone defect model further confirmed better vascularized bone regeneration in 3D-printed SZP scaffolds. These findings indicate that the proposed 3D-printed SZP scaffolds might be a versatile candidate for bone tissue engineering.

10th Anniversary Statement

Journal of Materials Chemistry B covers high-quality studies across multiple topic areas in materials chemistry with a focus on applications in biology and medicine including ''bioactive materials and regenerative medicine'', which is also our main research interest. Our first paper was published in the *Journal of Materials Chemistry B* almost 10 years ago when the *Journal of Materials Chemistry* was decomposed into part A, B and C in 2013, and more than 20 papers have been submitted and published in the *Journal of Materials Chemistry B* in these 10 years. We are proud to have so long a history in cooperation with such an excellent journal as well as its preeminent community and witnessed the development of the journal with increased impact and quality. The best way to express our gratitude is to continue to interact closely with the community and report our significant research advances such as this newly investigated multi-functional strontium–zinc-phosphate bioceramic. Based on our studies in the last 10 years, we believe this kind of bioactive inorganic material has great potential for regenerative medicine and disease therapy in the future. Congratulations on the 10th anniversary and best wishes to the *Journal of Materials Chemistry B*.

1. Introduction

Bone defects are traditionally repaired by conventional therapy including autografting and allografting, which are limited due to scarce availability, or risk of immunoreaction and disease transmission, respectively.[1] Therefore, artificial biomaterials are developed for the reconstruction of bone defects owing to their easy availability and great formability.[2–5] Among them,

[a] *College of Chemistry and Chemical Engineering, Donghua University, Shanghai, 201620, China*

[b] *Zhejiang Engineering Research Center for Tissue Repair Materials, Wenzhou Institute, University of Chinese Academy of Sciences, Wenzhou, 325000, China.*
  E-mail: jchang@mail.sic.ac.cn, cryangchen@ucas.ac.cn

[c] *Joint Centre of Translational Medicine, The First Affiliated Hospital of Wenzhou Medical University, Wenzhou, 325000, China*

[d] *College of Biological Science and Medical Engineering, Donghua University, Shanghai, 201620, China. E-mail: synicn@dhu.edu.cn*

[e] *Department of Orthopaedics, The First Affiliated Hospital of Wenzhou Medical University, Wenzhou, 325000, China*

[f] *Shanghai Institute of Ceramics, Chinese Academy of Sciences, Shanghai, 200050, China*

[g] *College of Materials Science and Opto-electronic Technology, University of Chinese Academy of Sciences, Beijing, 100049, China*

† Electronic supplementary information (ESI) available. See DOI: **https://doi.org/10.1039/d2tb02614g**

‡ These authors have contributed equally to this work and share the first authorship.

This journal is © The Royal Society of Chemistry 2023

J. Mater. Chem. B, 2023, 11, 5469–5482 | 5469

calcium phosphate (CaP) bioceramics, such as tri-calcium phosphate (TCP) and hydroxyapatite (HA) are commonly employed as bone grafting materials clinically due to their chemical resemblance to native bone.[6] However, these CaP bioceramics show scanty osteogenic promotion ability and lack the capacity of other biological functions (*e.g.*, angiogenesis, osteoimmunomodulation and anti-bacterial activity), making it hard to repair bone defects in complex conditions such as ischemia or infection. Thus, it is of great importance to improve the biological activities of CaP bioceramics to meet the variety of clinical demands in bone tissue engineering applications.

Metal ion doping in CaP bioceramics is one of the most direct and efficient approaches to improve their bioactivity for bone regeneration. Different metal elements possess different biological functions. For instance, trace element strontium (Sr) is able to stimulate new bone formation by promoting the activity of osteoblasts and endothelial cells, and inhibiting the activity of osteoclasts, showing enhanced osteogenic and angiogenic ability.[7–9] Sr-doped CaP bioceramics have been found to create an osteogenic microenvironment *via* provoking osteogenic differentiation of bone marrow mesenchymal stem cells (BMSCs), and improving early angiogenesis.[10] In contrast, trace element zinc (Zn) not only plays a pivotal role in skeletal development and bone growth, but also possesses anti-inflammatory and anti-bacterial properties.[11,12] Zn-doped CaP bioceramics can therefore increase bone repair through directly regulating bone relative cells or triggering the macrophage-mediated osteoimmunomodulation, and prevent bacterial infection when implanted in bone defects.[13–16] More interestingly, the incorporation of Sr and Zn together would further boost the efficiency of bone repair, presenting a synergistic effect on bone regeneration.[17–19] Although the ion substitution method is an available strategy for enriching biological functions of CaP bioceramics, it cannot precisely control the constituents of synthesized bioceramics and the distribution of doped ions, especially for more than one ion doping, which probably causes poor repeatability and unstable material functions. In contrast, single-phased bioceramics with a fixed composition have strong controllability and stability, indicating large potential in clinical translational application.

Inspired by these findings, we speculated that single-phased phosphate bioceramics containing both Sr and Zn possess multiple biological functions beneficial for bone tissue engineering including osteogenesis, angiogenesis and immunomodulation, and anti-bacterial activity. To clarify this, we first synthesized a Sr–Zn-phosphate (SZP, $SrZn_2(PO_4)_2$) bioceramic and fabricated SZP porous scaffolds using a three-dimensional (3D) printing technique. Furthermore, β-TCP scaffolds with the same 3D printed structure were prepared as a control to systemically examine the physicochemical properties (*e.g.*, mechanical properties, degradation rate and ion release) and biological effects (osteogenesis, angiogenesis, macrophage-mediated immunomodulation and anti-bacterial activity) *in vitro*. Finally, we validated the potential of 3D printed SZP scaffolds for bone restoration *in vivo* using a rat skull defect model (Fig. 1).

2. Materials and methods

2.1. Materials

All chemicals were purchased from Aladdin Reagent Co., Ltd. (Shanghai, China) except those otherwise mentioned. α-minimum
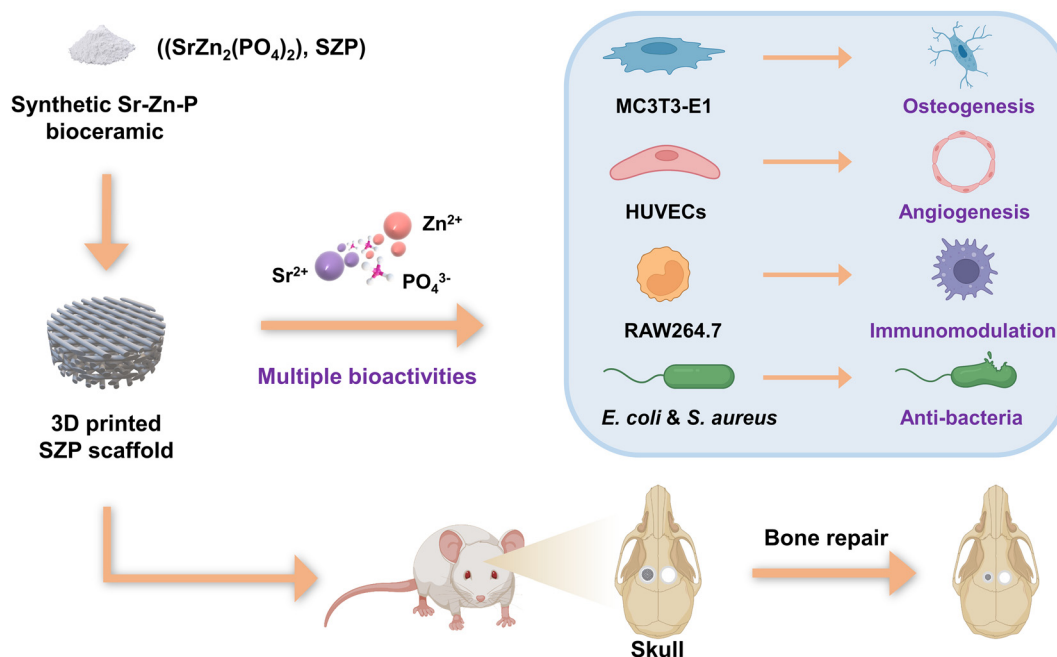

Fig. 1 Schematic diagram of the development of 3D printed SZP scaffolds with multiple bioactivities.

5470 | *J. Mater. Chem. B*, 2023, **11**, 5469–5482

This journal is © The Royal Society of Chemistry 2023

essential medium (α-MEM) was purchased from Zhejiang Jinuo Biomedical Technology Co., Ltd (Zhejiang, China). Dulbecco's modified Eagle's medium high-glucose (DMEM) was purchased from Servicebio Technology Co., Ltd (Wuhan, China). Fetal bovine serum (FBS) was bought from ExCell Bio Co., Ltd (Zhejiang, China). Penicillin, streptomycin and cell counting kit-8 (CCK-8) were purchased from Yeasen Biotechnology Co., Ltd (Shanghai, China). An alkaline phosphatase (ALP) assay kit and bicinchoninic acid (BCA) protein assay kit were bought from Beyotime Biotechnology Co., Ltd (Shanghai, China). ALP staining kit was purchased from Beijing Solaibio Technology Co., Ltd (Beijing, China). Matrigel was bought from Shanghai Nova Pharmaceutical Technology Co., Ltd (Shanghai, China). All antibodies were purchased from Dakewei Biotechnology Co., Ltd (Biolegend, USA).

2.2. Synthesis and characterization of SZP powders

SZP powders were synthesized by a solution combustion method.[20] Briefly, 0.01 mol Sr nitrate ($Sr(NO_3)_2$), 0.02 mol Zn nitrate hexahydrate ($Zn(NO_3)_2 \cdot 6H_2O$), 0.02 mol diammonium hydrogen phosphate ($(NH_4)_2HPO_4$) and 0.03 mol urea ($CO(NH_2)_2$) were added to 100 mL distilled water, and mixed for 1 h at room temperature to form transparent solution. After this, the solution was heated at 550 °C for 5 h in a furnace (KSL-1200X, Hefei Kejing Material Technology Co., Ltd, China) with a heating rate of 2 °C min^{-1}, which was followed by grinding and sieving to 300-mesh to get SZP powders. The obtained SZP powders were characterized with an X-ray diffractometer (XRD, Bruker, Germany) using Cu Kα radiation operating at a voltage of 40 kV with a current of 40 mA.

2.3. Fabrication and characterization of SZP scaffolds

To fabricate SZP scaffolds, injectable inks were prepared by mixing 0.2 g SZP powders with 0.1 g sodium alginate and 1.7 mL 20 wt% F127. After being loaded into the printing tubes, 3D SZP scaffolds with a lay-down pattern of 45° were printed using an extrusion-based 3D printer (BioMaker 4, SunP, China) with an extrusion speed of 0.5 mm^3 s^{-1} and a moving speed of 5 mm s^{-1}. As a control, 3D β-TCP scaffolds were printed with the same settings. After being dried at 60 °C for 24 h, the printed 3D SZP and β-TCP scaffolds were sintered. Based on the published work, β-TCP scaffolds were sintered at 1100 °C for 3 h with a heating rate of 2 °C min^{-1}.[21] To optimize the calcination temperature, the SZP scaffolds were calcined at 800 °C, 900 °C and 1000 °C for 3 h at the same heating rate. For in vivo experiments, 3D printed SZP and β-TCP scaffolds were cut into a cylinder shape ($\varnothing$ 5 mm × 1 mm) due to the requirement of the animal model.

The 3D printed scaffolds were photographed using an optical microscope (Ckx53, Olympus, China). The surface morphology and elemental distribution of SZP scaffolds were examined using a scanning electron microscope with an energy dispersive spectroscope (SEM-EDS, SU8010, HITACHI, Japan; EDS, Phenom Pharos, Phenom, Netherland). The porosity of the scaffolds was measured by the water displacement approach, where the porosity (P) was calculated based on the weights of dried (W_1), water-filled (W_2) and buoyant (W_3)

scaffolds.[22] The porosity (P) was determined using the following equation:

$$P = (W_2 - W_1)/(W_2 - W_3) \times 100\%$$

The mechanical properties of the 3D printed scaffolds were examined using a universal testing machine (5944 MicroTester, Instron, USA). To quantify the ion release rate, scaffolds were soaked in Tris–HCl solution (pH = 7.4) at a ratio of 10 mg mL^{-1} and shocked at 37 °C for 1, 3, 7, 14 and 21 days, respectively, and the immersion solutions were collected at each time point for the measurement of Zn^{2+}, Sr^{2+} and PO_4^{3-} using inductively coupled plasma-mass spectrometry (ICP-MS, Agilent 7850, Singapore). Meanwhile, the degradation ratio of the scaffolds was determined by the weight reduction of SZP scaffolds during soaking.

2.4. Effect of 3D printed SZP scaffolds on osteogenesis in vitro

Cell culture: mouse embryonic osteoblast precursor cells (MC3T3-E1) were purchased from the cell bank of the Chinese Academy of Sciences. MC3T3-E1 were cultured in α-MEM with the addition of 10% FBS, 100 U per mL penicillin and 100 mg per mL streptomycin in humidified 5% CO_2/95% air at 37 °C.

Cell proliferation: MC3T3-E1 cells were seeded on the 3D printed scaffolds in a 48-well plate with 2×10^3 cells per well and cultured for 1, 3 and 5 days (i.e. Day 1, Day 3 and Day 5). The culture medium was replaced every other day. At each time point, the culture medium was replaced with 300 μL per well mixture of α-MEM and CCK-8 at the ratio of 9 : 1. After incubation at 37 °C for 1 h, 100 μL of liquid was moved to a 96-well plate from each well, and the absorbance was detected using a microplate reader (EPOCH2NS, BioTek, USA) at a wavelength of 450 nm for the evaluation of MC3T3-E1 cell proliferation.

ALP staining and activity: MC3T3-E1 cells were seeded onto the 3D printed scaffolds which were located in a 48-well plate with 1×10^4 cells per well. The cells were cultured for 7 days with the culture medium changed every other day. For ALP staining, samples were washed with PBS three times, followed by a 10 min fixation with 4% paraformaldehyde and a 30 min incubation with an ALP staining kit. For the ALP activity assay, cells were then cleaved with 100 μL enzyme-free lysis solution and collected into 1.5 mL EP tubes. After centrifugation at 12 000 rpm for 3 min, the supernatant was collected into new EP tubes. According to the manufacturer's instructions, 20 μL of the supernatant was taken to quantify the enzyme using the ALP test kit and to determine the protein content using the BCA protein concentration determination kit, respectively. The ALP activity analysis was normalized by the total protein measured using a BCA protein assay kit.

Osteogenic gene expression: MC3T3-E1 cells were seeded into the 3D printed scaffolds present in a 6-well plate with 2×10^5 cells per well. After 7 days, total RNA was extracted from the MC3T3-E1 cells for mRNA expression analysis of osteogenic factors including ALP, osteocalcin (OCN), bone morphogenetic protein 2 (BMP-2) and runt-related transcription factor 2 (RUNX-2) using a real-time polymerase chain reaction (RT-PCR) and PCR MasterMix (SYBR Green, Yeasen, China). The gene expression was normalized by glyceraldehyde-3-phosphate

This journal is © The Royal Society of Chemistry 2023

J. Mater. Chem. B, 2023, **11**, 5469–5482 | **5471**

dehydrogenase (GAPDH) and the relative quantification of gene expression was calculated according to the $2^{-\Delta\Delta CT}$ method.[23] All primer sequences are listed in Table S1 (ESI†).

2.5. Effect of 3D printed SZP scaffolds on angiogenesis *in vitro*

Cell culture: human umbilical vein endothelial cells (HUVECs) were purchased from EK-Bioscience Biotechnology Co., Ltd (Shanghai, China), and cultivated in DMEM including 10% FBS, 100 U per mL penicillin and 100 mg per mL streptomycin in humidified 5% CO_2/95% air at 37 °C.

Cell proliferation: HUVECs were seeded on the 3D printed scaffolds placed in a 48-well plate with 1×10^3 cells per well and cultivated for 1, 3 and 5 days (*i.e.* Day 1, Day 3 and Day 5). The culture medium was changed every other day. Similar to the examination of the MC3T3-E1 cell proliferation, the proliferation of HUVECs was also estimated using a microplate reader after incubation with CCK-8.

Cell migration: HUVECs were seeded in a 6-well plate with 4×10^5 cells per well and cultured in humidified 5% CO_2/95% air at 37 °C for 12 h. Then, a straight "scratch" was created with a p200 pipet tip according to the publication,[24] followed by the "scratch" quantification (original state), or co-culturing with scaffolds for another 24 h (final state). Optical microscopy was performed to record the "scratches" from the original and final states following washing with PBS, fixation with 4% paraformaldehyde and staining with methyl violet, where the original (A_o) and final (A_f) areas of the "scratches" were acquired using ImageJ (National Institutes of Health, USA). The migration rate (ξ) was computed using the following formula:

$$\xi = (A_o - A_f)/A_o \times 100\%$$

Tube formation: the Matrigel was placed in an ice box and thawed at 4 °C. The melted Matrigel was then added to a pre-cooled 48-well plate (120 µL per well) and incubated at 37 °C for 30 min. HUVECs were seeded into the 48-well plate with a density of 6×10^4 cells per well and scaffolds were added to the well plate. After culture at 37 °C for 4 h, the formed tubes were observed by microscopy, and the catheter length was calculated using ImageJ software.

Angiogenic gene expression: HUVECs were seeded in a 6-well plate with 2×10^5 cells per well and co-cultured with SZP/β-TCP scaffolds for 3 days. After then, the culture medium was collected for mRNA expression analysis of vascular endothelial growth factor (VEGF), endothelial nitric oxide synthase (eNOS), basic fibroblast growth factor (bFGF) and hypoxia inducible factor 1α (HIF-1α) using the same method described earlier. The primers are listed in Table S1 (ESI†).

2.6. Effect of 3D printed SZP scaffolds on macrophage-mediated immunomodulation

Cell culture: mouse-derived macrophage cell line RAW264.7 cells were purchased from the cell bank of the Chinese Academy of Sciences. The RAW264.7 cells were cultivated in DMEM supplemented with 10% FBS, 100 U per mL penicillin and 100 mg per mL streptomycin in humidified 5% CO_2/95% air at 37 °C.

Inflammatory gene expression: RAW264.7 cells were seeded on the 3D printed scaffolds present in a 6-well plate at a density of 2×10^4 cells per cm^2 and cultured for 2 days, which was followed by mRNA analysis of pre-inflammatory factors interleukin (IL)-1β, tumor necrosis factor α (TNF-α) and inducible nitric oxide synthase (iNOS), and anti-inflammatory factors transforming growth factor 1 beta (TGF-1β), recombinant interleukin-1 receptor antagonist (IL-1rα) and mannose receptor (CD206). The primers are listed in Table S1 (ESI†).

Macrophage-mediated osteogenesis and angiogenesis: the culture medium collected from the above studies was filtered with a 0.22 µm filter membrane and mixed with an equal volume of α-MEM or DMEM and presented as the conditioned medium to culture MC3T3-E1 cells and HUVECs for the estimation of macrophage-mediated effect on osteogenesis and angiogenesis, respectively.

2.7. Effect of 3D printed SZP scaffolds on anti-bacterial activity

To estimate the anti-bacterial ability of the 3D printed scaffolds, 300 µL *Staphylococcus aureus* (*S. aureus*) and *Escherichia coli* (*E. coli*) at a density of 1×10^6 CFU mL^{-1} were co-cultured with the scaffolds at 37 °C for 24 h, respectively. As the blank controls, *S. aureus* and *E. coli* were cultured at 37 °C for 24 h without scaffolds. Subsequently, the bacterial liquid was collected and diluted to 1% with saline, and 20 µL diluted bacterial liquid was added to Luria–Bertani (LB) agar plates for another 18 hour culture at 37 °C. The number of colonies was assessed using an automatic colony counter (Icount 22, Hangzhou Shineso Technology Co., Ltd, China). Based on the number of colonies on LB agar plates from the blank controls (B) and scaffolds (S), the survival rate (η) of bacteria was calculated with the formula below:

$$\eta = S/B \times 100\%$$

2.8. Effect of SZP scaffolds on bone regeneration *in vivo*

Animal model: skeletal mature male Sprague-Dawley (SD) rats were purchased from the Zhejiang Provincial Laboratory Animal Center, and the whole animal experiments were approved by the Animal Research and Ethics Committee of Wenzhou Institute of University of Chinese (WIUCAS21101831). The cranial bone defect model was created using the published approach.[7] Briefly, rats were generally and deeply anesthetized, and the scalp was opened with surgical scissors to expose the calvarium. Bilateral skull critical-sized defects were established by drilling two full-thickness 5 mm-diameter holes using a trephine. After this, the created bone defects were left untreated (Blank), or implanted with SZP or β-TCP scaffolds, which was followed by wound suturing to end the surgery.

Micro-computed tomography (micro-CT) and histological analysis: 4 weeks after the surgery, all rats were sacrificed and their skulls were collected. After fixation with 4% paraformaldehyde, the collected bone samples were imaged with micro-CT (Bruker, Germany). Bone mineral density (BMD) and bone volume fraction (bone volume/tissue volume, BV/TV) were quantified using the manufacturer's analysis software (CTAn,

5472 | *J. Mater. Chem. B*, 2023, **11**, 5469–5482

This journal is © The Royal Society of Chemistry 2023

Version 1.15.4.0, Germany). Subsequently, bone samples were decalcified with ethylenediaminetetraacetic acid (EDTA) and embedded in paraffin for the preparation of 4 μm-thick sections. These sections were subjected to hematoxylin–eosin (H&E) staining, Masson's trichrome staining, or immunohisto-chemical staining for platelet endothelial cell adhesion molecule-1 (PECAM-1, CD31) and OCN.

2.9. Statistical analysis

The analysis was conducted using GraphPad software (GraphPad Prism 8, USA), and a two-sided unpaired Student's *t*-test was used to analyze data between the two groups. Otherwise, a one-way

analysis of variance (ANOVA) was performed to test the differences between groups ($n \geq 3$). All the data are presented by mean $\pm$ SEM and the significance level for all tests was $P < 0.05$.

3. Results

3.1. Characterization of SZP powders and 3D-printed SZP scaffolds

SZP powders were first synthesized by a solution combustion method. The crystal structure of the synthesized powders was identified as pure SZP by the XRD patterns (JCPDS Card No.
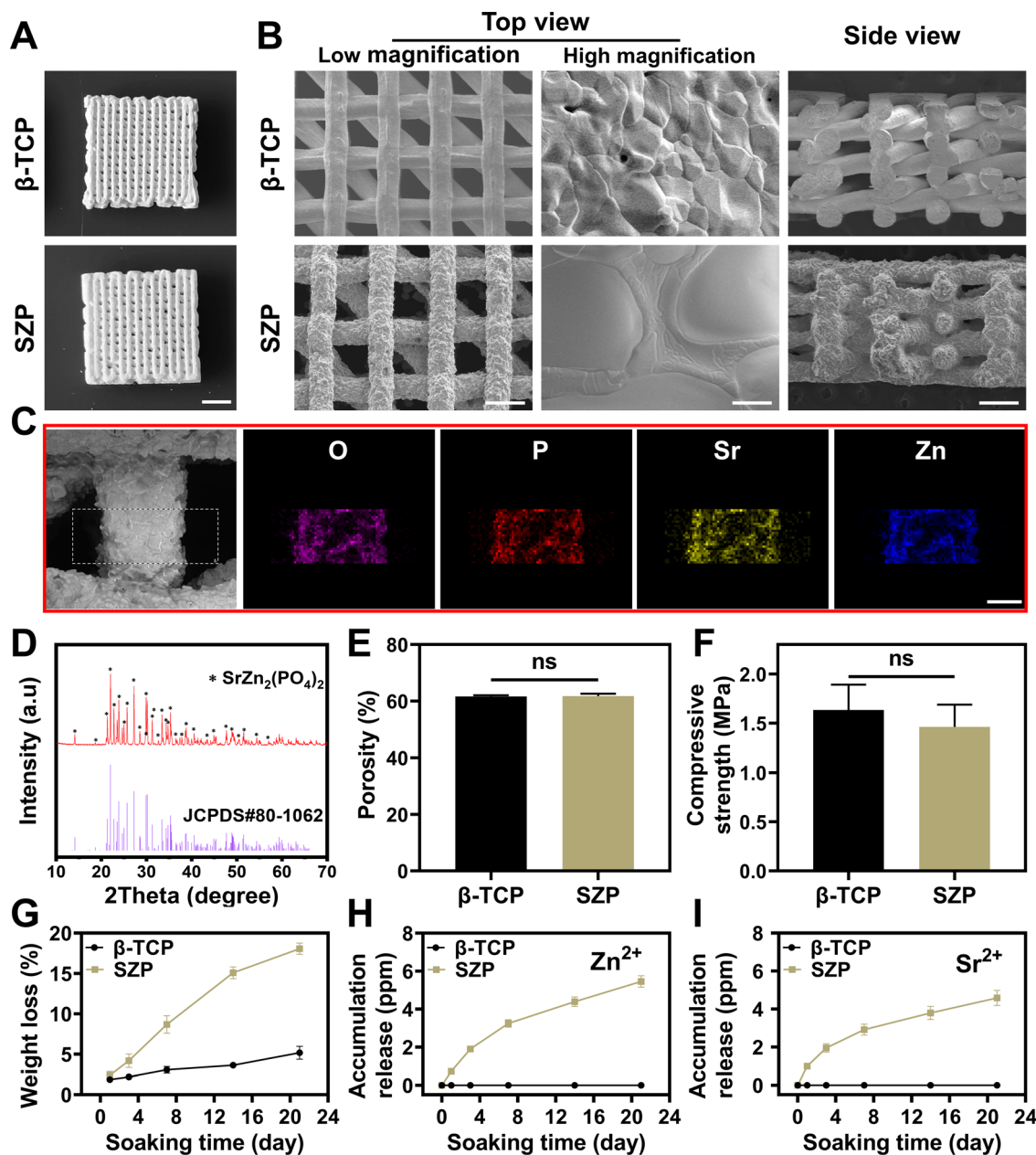

Fig. 2 Characterization of 3D printed SZP and β-TCP scaffolds. (A) Optimal images. Scale bar: 2 mm. (B) SEM characterization. Scale bar: 400 μm (low magnification and side view); 4 μm (high magnification). (C) EDS characterization. Scale bar: 100 μm. (D) XRD characterization. (E) Porosity ($n = 4$). (F) Compressive strength ($n = 3$). (G) Degradation ($n = 3$). (H) Zn^{2+} and (I) Sr^{2+} release profiles ($n = 3$). ns: no significant difference.

This journal is © The Royal Society of Chemistry 2023

J. Mater. Chem. B, 2023, 11, 5469–5482 | 5473

80-1062, Fig. S1A, ESI†). The SEM images showed that SZP powders were stone-shaped with an estimated particle size of 2–30 μm (Fig. S1B, ESI†). Furthermore, SZP scaffolds were prepared by the 3D printing technique and sintered at different temperatures (800 °C, 900 °C and 1000 °C). The SEM images showed that the density and structural homogeneity of the scaffolds increased with temperature (Fig. S2, ESI†), and SZP scaffolds calcined at 1000 °C were chosen for the following experiments. To better evaluate the physicochemical properties of the scaffolds, 3D printed β-TCP scaffolds following the same procedure were set as controls. The optimal photos displayed that both 3D printed SZP and β-TCP scaffolds possessed uniform porous structures (Fig. 2A), which were 3D interconnected with a pore size of approximately 350 μm × 300 μm from the top view and 277 μm × 176 μm from the side view (Fig. 2B). Larger crystals and rougher macrostructural surface were observed on SZP scaffolds compared with β-TCP scaffolds. EDS analysis validated the component of SZP as the existence of oxygen, phosphorus, Zn and Sr elements on the SZP scaffolds (Fig. 2C), which was further confirmed as SZP crystals by XRD analysis (Fig. 2D). Equivalent porosity ($61.78 \pm 0.85\%$ versus $61.64 \pm 0.43\%$), compressive strength (1.46 ± 0.23 MPa versus 1.63 ± 0.26 MPa) and Young's modulus (55.97 ± 6.06 MPa versus 55.51 ± 10.88 MPa) were observed in the SZP and β-TCP scaffolds, respectively (Fig. 2E, F, and Fig. S4, ESI†). The in vitro degradation study showed that both SZP and β-TCP scaffolds presented sustained weight loss with the increase of the soaking time, and SZP scaffolds showed faster weight loss than β-TCP scaffolds (Fig. 2G). Meanwhile, the ion release profile in Fig. 2H, I and Fig. S3 (ESI†) revealed the sustained release of

Zn^{2+}, Sr^{2+} and PO_4^{3-} from SZP scaffolds and Ca^{2+} and PO_4^{3-} from β-TCP scaffolds. All these results demonstrated the successful fabrication of the 3D-printed SZP scaffolds.

3.2. Effect of 3D printed SZP scaffolds on osteogenesis

The proliferation of MC3T3-E1 cells cultured on different scaffolds was first evaluated using the CCK-8 assay. As shown in Fig. 3A, cells proliferated on both 3D printed β-TCP and SZP scaffolds from Day 1 to Day 5, while a significantly higher proliferation was observed on Day 3 in the SZP group as compared to the β-TCP group. Then, the ALP activity in MC3T3-E1 cells cultured on β-TCP or SZP scaffolds for 7 days was detected, which revealed that more ALP ($\sim$1.32-fold) expressed in cells stimulated by SZP scaffolds compared with those stimulated by β-TCP scaffolds (Fig. 3B and C). Furthermore, the RT-PCR study revealed that MC3T3-E1 cells co-cultured with SZP scaffolds had significantly higher gene expression of osteogenic factors including BMP-2 ($\sim$1.84-fold), ALP ($\sim$1.85-fold), RUNX-2 ($\sim$1.35-fold) and OCN ($\sim$2.47-fold) as compared to the cells co-cultured with β-TCP scaffolds for 7 days (Fig. 3D).

3.3. Effect of 3D printed SZP scaffolds on angiogenesis

Similar to MC3T3-E1 cells, HUVECs also proliferated well on both the 3D printed β-TCP and SZP scaffolds with time, and a significantly higher proliferation of HUVECs was observed on SZP scaffolds as compared to β-TCP scaffolds on Day 5 (Fig. 4A). The cell migration study revealed that after co-cultured for 24 h, SZP scaffolds led to faster migration of HUVECs across a "scratch" than β-TCP scaffolds, with a migration rate of
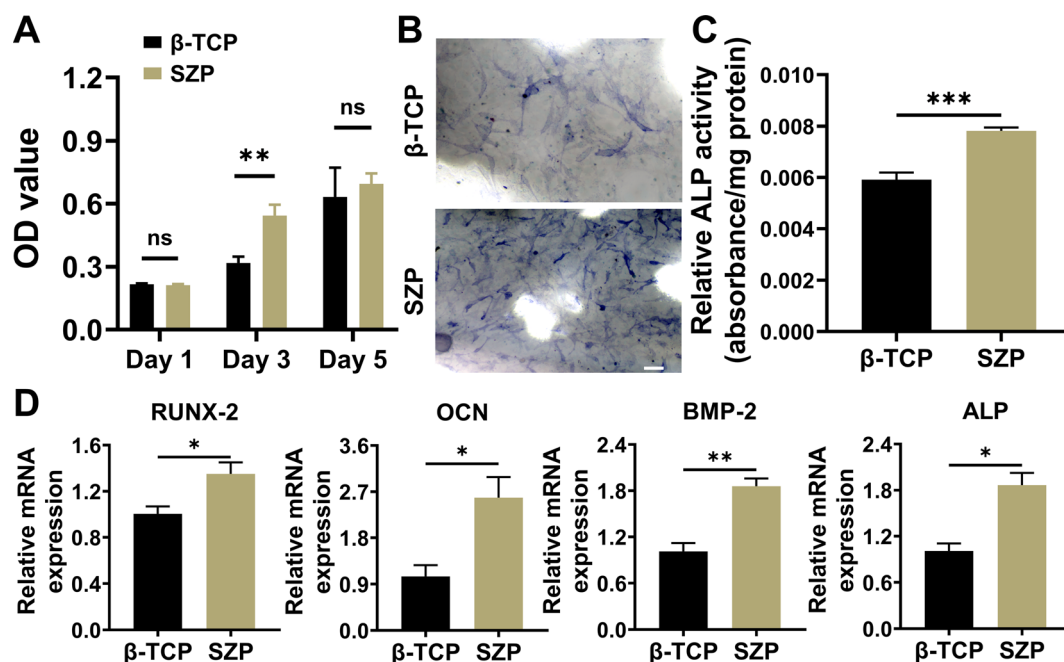

Fig. 3 Effect of 3D printed SZP scaffolds on the proliferation and differentiation of MC3T3-E1 cells. (A) The proliferation of MC3T3-E1 cells co-cultured with SZP or β-TCP scaffolds for 1, 3 and 5 days (n = 4). (B) ALP staining and (C) ALP activity in MC3T3-E1 cells after culturing on different scaffolds for 7 days (n = 6). Blue color represents ALP. Scale bar: 100 μm. (D) The expression of osteogenic genes (RUNX-2, OCN, BMP-2 and ALP) in MC3T3-E1 cells after treatment with different scaffolds for 7 days (n = 3). *$P < 0.05$, **$P < 0.01$, ***$P < 0.001$, ns: no significant difference.

39.92 ± 1.76% and 32.38 ± 1.89%, respectively (Fig. 4B and C). Besides, HUVECs co-cultured with SZP scaffolds formed more tubes than those with β-TCP scaffolds, which was quantitatively reflected by a longer tube length (Fig. 4D and E) and more branch points (Fig. S5A, ESI†). Furthermore, the angiogenic gene expresssions of bFGF, eNOS, HIF-1α and VEGF in HUVECs cultured on SZP scaffolds for 3 days were significantly higher or prone to be higher than those on β-TCP scaffolds (Fig. 4F).

3.4. Effect of 3D printed SZP scaffolds on macrophage polarization

Compared with β-TCP scaffolds, SZP scaffolds exhibited higher ability in downregulating the gene expression of inflammatory factors including IL-1β, TNF-α and iNOS, while upregulating the gene expression of anti-inflammatory factors including TGF-1β, IL-1rα and CD206 in RAW264.7 macrophages, displaying the ability to stimulate macrophage towards the M2 type. (Fig. 5A and B).

3.5. Effect of 3D printed SZP scaffolds on macrophage-mediated osteogenesis

To evaluate macrophage-mediated osteogenesis, conditioned media from the incubation of RAW264.7 macrophages treated with different scaffolds were prepared for the MC3T3-E1 cell culture. As shown in Fig. 6A, MC3T3-E1 cells continuously proliferated in both macrophage/β-TCP and macrophage/SZP conditioned medium, and significantly greater cell proliferation was exhibited in the macrophage/SZP group as compared to the macrophage/β-TCP group from Day 3 to Day 5. After culturing for 7 days, higher ALP activity (∼1.30-fold) was observed in MC3T3-E1 cells cultured in the macrophage/SZP conditioned medium compared with the cells cultured in the macrophage/β-TCP conditioned medium (Fig. 6B and C). Additionally, compared to the macrophage/β-TCP conditioned medium, the macrophage/SZP conditioned medium led to significantly higher gene expression of

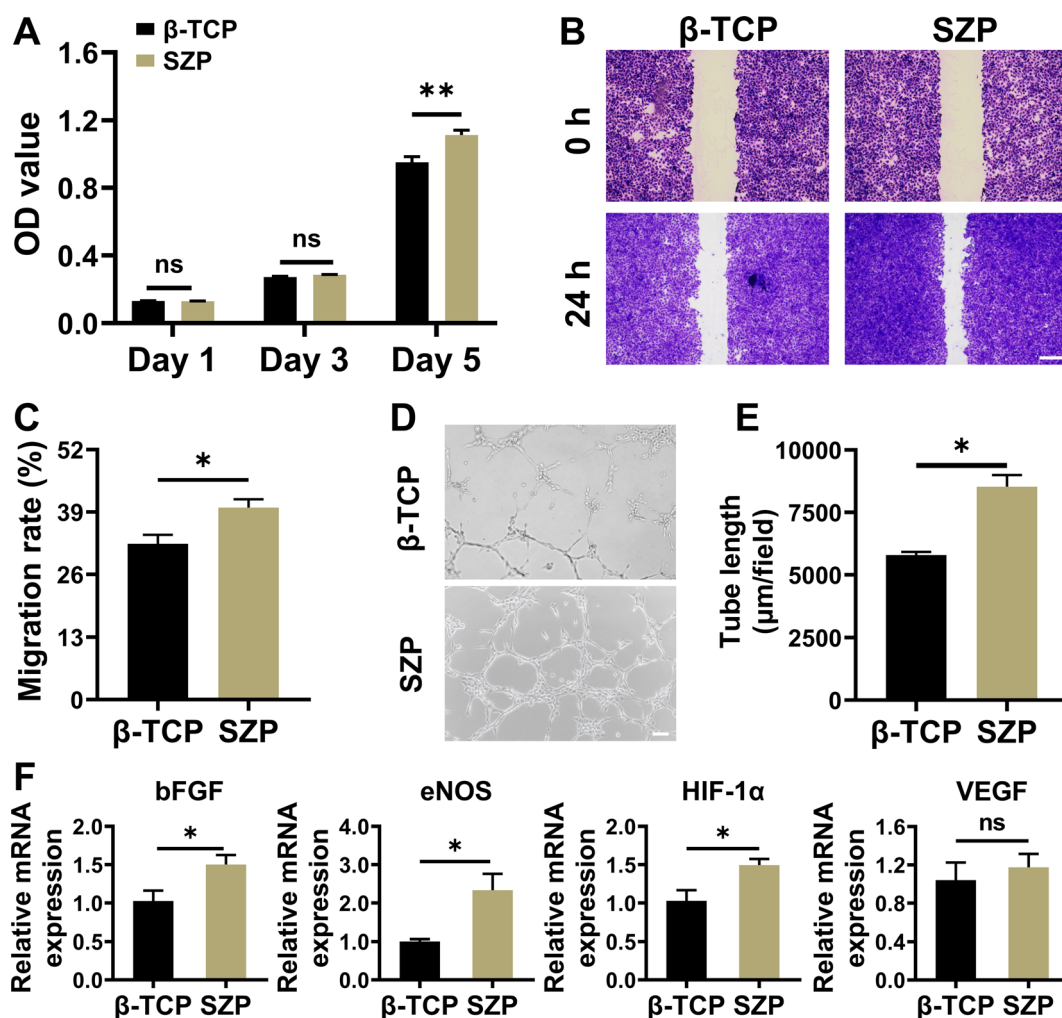**Fig. 4** Effect of 3D printed SZP scaffolds on the proliferation, migration, differentiation and tube formation of HUVECs. (A) CCK-8 assay of the proliferation of HUVECs co-cultured with scaffolds for 1, 3 and 5 days ($n = 6$). (B) Representative images of cell migration and (C) quantitative analysis of cell migration rate after 24 h of culture ($n = 6$). Scale bar: 400 μm. (D) Representative images and (E) quantitative analysis of *in vitro* tube formation after 4 h of culture ($n = 4$). Scale bar: 400 μm. (F) The angiogenic genes (bFGF, eNOS, HIF-1α, VEGF) expression in HUVECs after 3 days of culture on different scaffolds ($n = 4$). *$P < 0.05$, **$P < 0.01$, ns: no significant difference.
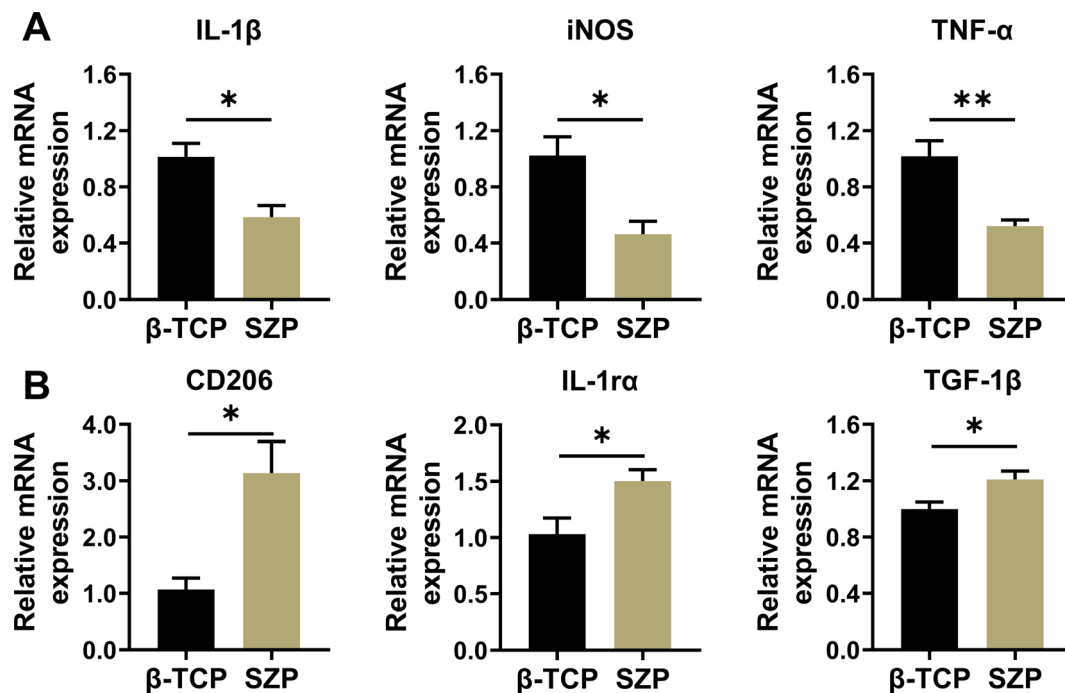
This journal is © The Royal Society of Chemistry 2023

J. Mater. Chem. B, 2023, **11**, 5469–5482 | **5475**

Fig. 5 Effect of SZP scaffolds on RAW264.7 macrophage polarization. Expression of (A) inflammatory genes of IL-1β, TNF-α and iNOS, as well as (B) anti-inflammatory genes of IL-1rα, CD206 and TGF-1β in RAW264.7 macrophages after a 3-day co-culture with SZP or β-TCP scaffolds ($n = 4$). *$P < 0.05$, **$P < 0.01$.
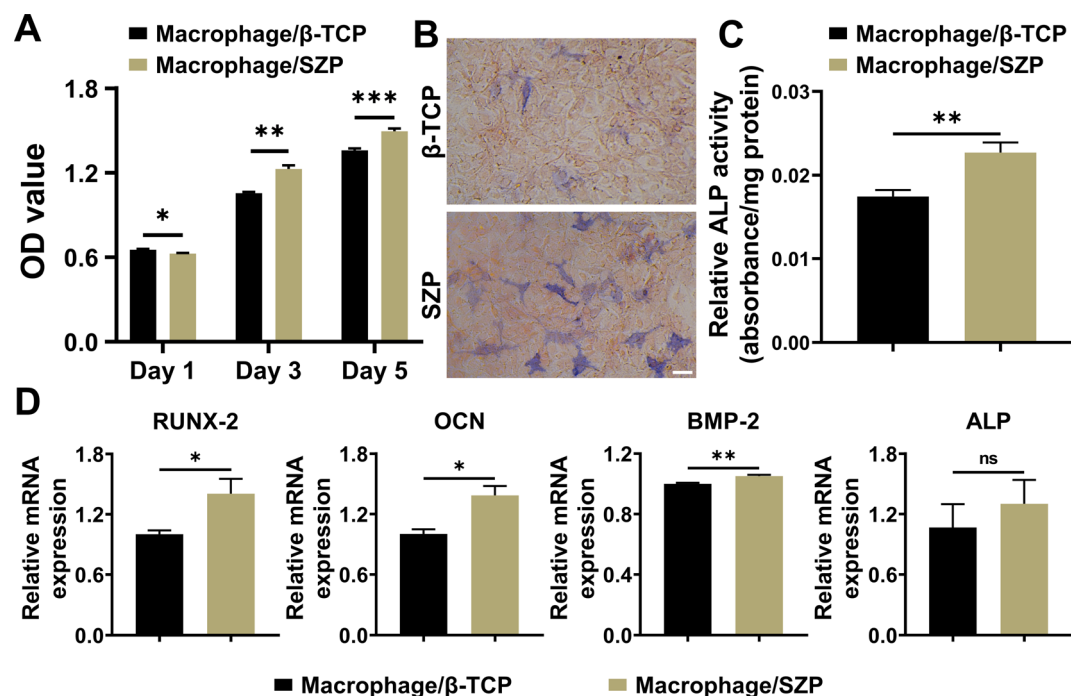

Fig. 6 Effect of the RAW264.7 macrophage/scaffolds conditioned medium on the proliferation and differentiation of MC3T3-E1 cells. (A) Cell proliferation in both macrophage/β-TCP and macrophage/SZP conditioned medium ($n = 6$). (B) ALP staining and (C) ALP activity in MC3T3-E1 cells after treatment with different conditioned medium for 7 days ($n = 6$). Blue color represents ALP. Scale bar: 100 μm (D) mRNA expression of osteogenic factors by MC3T3-E1 cells including RUNX-2, OCN, BMP-2 and ALP after 7 days of culture in the conditioned medium ($n = 4$). *$P < 0.05$, **$P < 0.01$, ***$P < 0.001$, ns: no significant difference.

osteogenic factors in MC3T3-E1 cells after 7 day culturing including OCN, BMP-2 and RUNX-2, while the gene expression of ALP tended to be higher but with no significant difference (Fig. 6D).

5476 | *J. Mater. Chem. B*, 2023, **11**, 5469–5482

This journal is © The Royal Society of Chemistry 2023

3.6. Effect of 3D printed SZP scaffolds on macrophage-mediated angiogenesis

After co-culturing with the macrophage/SZP or macrophage/β-TCP conditioned medium for 1, 3 and 5 days, HUVECs proliferated well with time and there was no difference in cell proliferation between the two culture states (Fig. 7A). However, HUVECs in macrophage/SZP conditioned medium exhibited stronger migration across the "scratch" when compared to HUVECs in the macrophage/β-TCP conditioned medium, with a migration rate of $66.08 \pm 1.84\%$ and $51.79 \pm 3.74\%$, respectively (Fig. 7B and C). In addition, compared to the macrophage/β-TCP conditioned medium, macrophage/SZP conditioned medium promoted more tube formation of HUVECs after cultured for 4 h (Fig. 7D), which was confirmed by the quantitative analysis of the tube length (Fig. 7E) and branch points (Fig. S5B, ESI†). Moreover, after culturing for 3 days,

HUVECs stimulated by the macrophage/SZP conditioned medium had significantly higher expression of angiogenic genes including VEGF, HIF-1α, and bFGF than HUVECs cultured in macrophage/β-TCP conditioned medium, while the gene expression of eNOS trended to be higher but with no significant difference (Fig. 7F).

3.7. Effect of 3D printed SZP scaffolds on anti-bacterial efficiency

As shown in Fig. 8, the anti-bacterial efficiency of the 3D printed scaffolds on both *S. aureus* and *E. coli* was detected. After co-culture with 3D printed β-TCP or SZP scaffolds for 24 h, the survival rate ($81.48 \pm 9.64\%$) of *S. aureus* in the β-TCP group was slightly lower than the Blank group without significant difference, while the survival rate ($16.85 \pm 5.94\%$) in the SZP group was significantly lower than that in both Blank and
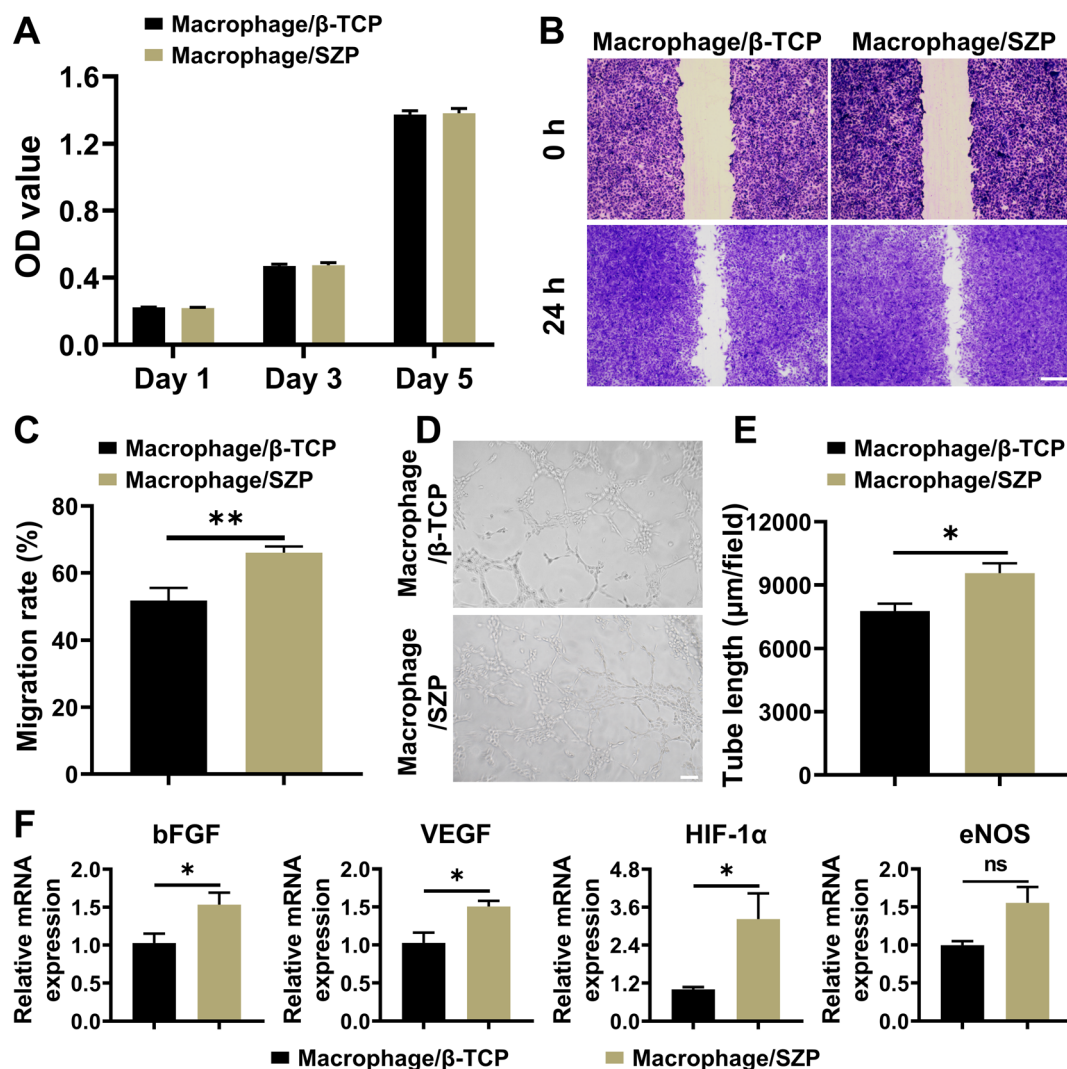

Fig. 7 Effect of RAW264.7 macrophages/scaffolds on the proliferation, migration, tube formation and differentiation of HUVECs. (A) Cell proliferation in both macrophage/β-TCP and macrophage/SZP conditioned medium ($n = 6$). (B) Representative images and (C) quantification of cell migration after 24 h culture in different conditioned medium ($n = 6$). Scale bar: 300 μm. (D) Representative images and (E) quantitative analysis of the *in vitro* tube formation of HUVECs after 4 h culture in different conditioned medium ($n = 4$). Scale bar: 200 μm. (F) The gene expression of angiogenic factors including VEGF, HIF-1α, eNOS and bFGF in HUVECs after 3 days of culture in different conditioned medium ($n = 4$). *$P < 0.05$, **$P < 0.01$, ns: no significant difference.
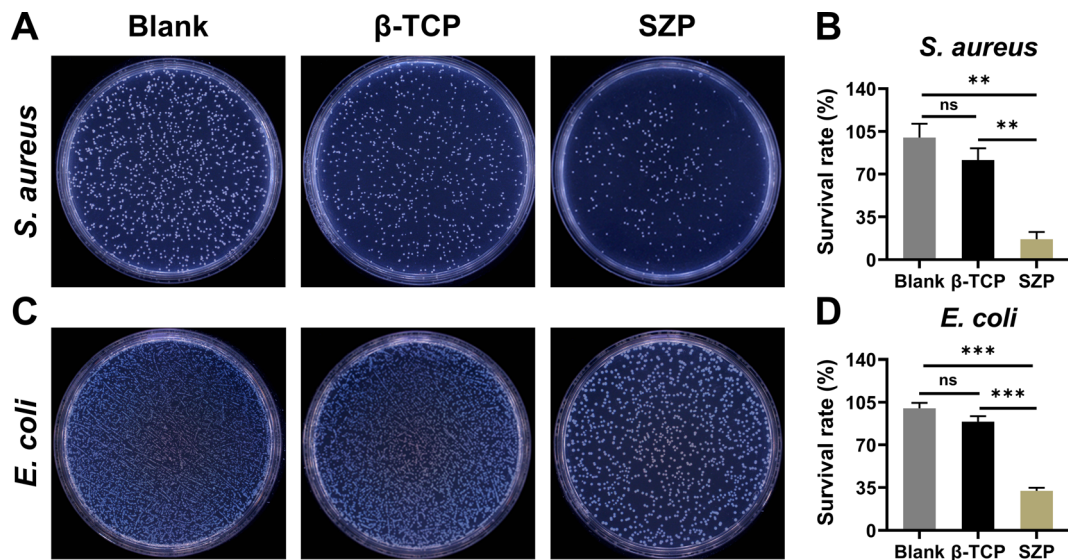
This journal is © The Royal Society of Chemistry 2023

J. Mater. Chem. B, 2023, **11**, 5469–5482 | **5477**

Fig. 8 Anti-bacterial analysis of SZP and β-TCP scaffolds against *S. aureus* and *E. coli*. (A) Representative images of *S. aureus* grown on agar plates after different treatments. (B) Quantification of the survival rate of *S. aureus* ($n = 3$). (C) Representative images of *E. coli* grown on agar plates after different treatments. (D) Quantification of the survival rate of *E. coli* ($n = 3$). $**P < 0.01$, $***P < 0.001$, ns: no significant difference.

β-TCP groups (Fig. 8A and B). Similar results were obtained in *E. coli* as the survival rates in the Blank, β-TCP and SZP groups were $100.00 \pm 4.41\%$, $89.04 \pm 4.52\%$ and $32.26 \pm 2.46\%$, respectively (Fig. 8C and D).

3.8. The effect of 3D printed SZP scaffolds on bone regeneration *in vivo*

Bone defects were created on skulls to evaluate the effect of 3D printed SZP scaffolds on bone regeneration *in vivo*. As shown in the 3D reconstructed micro-CT images (Fig. 9A), both the 3D printed β-TCP and SZP scaffolds promoted more new bone formation compared with the Blank group. However, more bone formation (green color) was observed after implantation of SZP scaffolds for 4 weeks as compared to the implantation of β-TCP scaffolds. Also, the degradation rate of SZP scaffolds *in vivo* seems faster than that of β-TCP scaffolds as the scaffold integrality was much better in the β-TCP group than that in the SZP group. The quantitative analysis further confirmed that SZP scaffolds resulted in a significantly higher BMD (~ 1.03-fold) and bone volume fraction (BV/TV) of newly formed bone inside the critical-sized bone defects, compared with β-TCP scaffolds (Fig. 9B and C), indicating the better bone repair ability.

The newly formed tissue was further estimated by the histological analysis including H&E staining and Masson's trichrome staining (Fig. 10A and B), which consistently showed that more newly formed tissues including collagen were observed in defects treated with 3D printed scaffolds as compared to the Blank group, and SZP scaffolds promoted more tissue regeneration than β-TCP scaffolds. Furthermore, the immunohistochemical staining of osteogenic biomarker OCN and angiogenic biomarker CD31 demonstrated that SZP scaffolds had higher bioactivity than β-TCP scaffolds to promote vascularized bone regeneration *in vivo* (Fig. 10C and D), with a

vascular number of 17.67 ± 0.33 and 11.67 ± 0.88, respectively (Fig. S6, ESI†).

4. Discussion

3D printing is widely utilized for bone graft fabrication owing to its structure controllability and reproducibility.[2,25] Equivalent mechanical properties have been proven between 3D printed β-TCP scaffolds and native trabecular bone,[26] while the proposed 3D printed SZP scaffolds in this study showed equivalent porosity, compressive strength and Young's modulus with 3D printed β-TCP scaffolds (Fig. 2 and Fig. S4, ESI†), indicating mechanical applicability of 3D printed SZP scaffolds. Notably, the pores inside the 3D printed scaffolds are three-dimensionally interconnected and highly oriented in this study, which mimics the porous network of the natural trabecular bone. Although other scaffold fabrication methods such as the freeze-drying method can also create interconnected and oriented pores, the pore controllability is far away from 3D printing.[27] The *in vitro* degeneration experiment showed a much faster weight loss and ion release rate in SZP scaffolds as compared to β-TCP scaffolds (Fig. 2 and Fig. S3, ESI†). This may be attributed to their larger microscopic surface area and different crystal structures as a much lower sintered temperature was required for SZP. However, such *in vitro* studies can only partially mimic the degradation process in the human body, thereby *in vivo* investigation is needed in further study. Since ions released from bioceramic scaffolds play crucial roles in new bone formation,[28] the capability of SZP scaffolds for sustained release of Sr^{2+}, Zn^{2+} and PO_4^{3-} were expected to have better tissue regeneration performance and more biological functions than β-TCP scaffolds with the limited release of Ca^{2+} and PO_4^{3-}, which was indeed proved in our following

5478 | *J. Mater. Chem. B*, 2023, **11**, 5469–5482
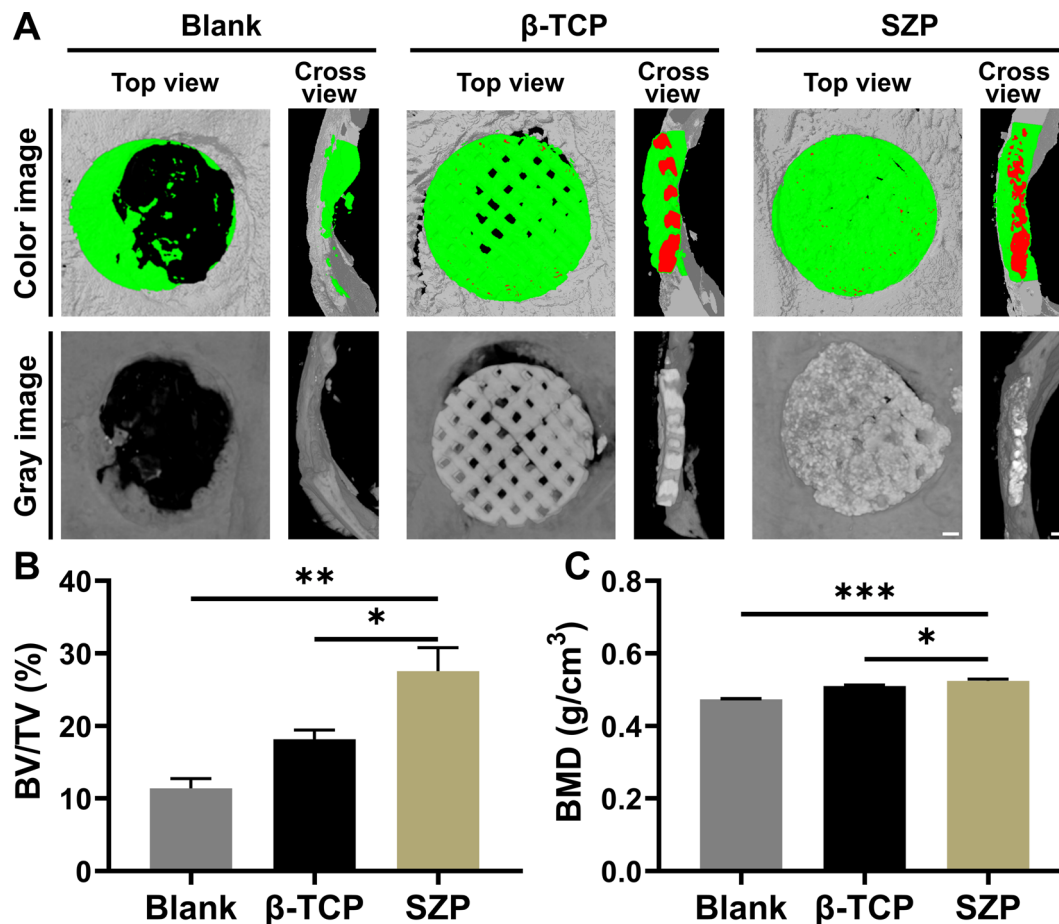
This journal is © The Royal Society of Chemistry 2023

Fig. 9 Micro-CT analysis of the microstructure of newly formed bone after the implantation of 3D printed SZP and β-TCP scaffolds into cranial bone defects in rats for 4 weeks. (A) Visualization of 3D reconstructed micro-CT images of newly formed bone (green color) and implanted scaffolds (red color). Scale bar: 1 mm. Quantitative analysis of (B) bone mineral density and (C) bone volume fraction (bone volume/tissue volume, BV/TV) of newly formed bone in the defects ($n = 4$). *$P < 0.05$, **$P < 0.01$, ***$P < 0.001$.

studies for the first time. Although other Sr/Zn containing biomaterials such as Sr/Zn dual ions-collagen co-assembly HA, Sr/Zn dual substituted CaP bioceramics or titanium alloy coated with Sr–Zn-P bioceramic mixture have been explored with multiple bioactivities for bone repair,[17–19,29] SZP scaffolds hold the advantages for clinical transformation due to the long-range ordered crystal structure of the single-phased SZP, which makes the scaffold's properties and functions super stable and sustainable. Specifically, 3D-printed SZP scaffolds exhibit multiple bioactivities including osteogenesis, angiogenesis, immunomodulation and anti-bacterial activity.

Osteogenic ability is also vital for an eligible bone graft.[30,31] β-TCP is widely used for bone grafting due to its compatibility, osteoconductivity, osteoinductivity and cell-mediated resorption.[32] In the current study, 3D printed β-TCP scaffolds were considered as the positive controls for the evaluation of 3D printed SZP scaffolds in the treatment of bone defects. Our results showed that SZP scaffolds induced higher proliferation of MC3T3-E1 cells and mRNA expression of osteogenic factors BMP-2, ALP, RUNX-2 and OCN than β-TCP scaffolds (Fig. 3). These *in vitro* results are validated by the animal experiments in

this study. The osteogenic function of SZP scaffolds was probably attributed to the released Sr and Zn. Specifically, the released ions may facilitate mineralization, which is a vital part of bone regeneration. For example, Sr–Zn silicate bioceramics reveal preferential Sr^{2+} release, which leads to higher pH and exhibits a superior potential in the formation of a mineralized layer.[33] The mineralized layer can further modulate the release of ions and the surrounding pH properly, which contributes to its global reassembly into peripheral phosphates in native bone. Besides, Sr ions are reported to stimulate osteoblast differentiation through activation of different signaling pathways including the Ras/MAPK or MAPK/Erk 1/2 signaling pathway, while Zn acts as a co-factor of alkaline phosphate,[9,34] contributing to bone mineralization. However, a high concentration of Zn^{2+} may cause cytotoxicity, which can be reduced by Sr^{2+} incorporation.[35] Sr/Zn substituted HA coatings were employed to improve the cytocompatibility and antimicrobial properties of the titanium alloy by plasma-spraying.[35] However, this enhancement is restricted to the surface of the titanium alloy and cannot be strictly controlled owing to the uncontrollable distribution of doped ions. Recently, Zn silicates have been
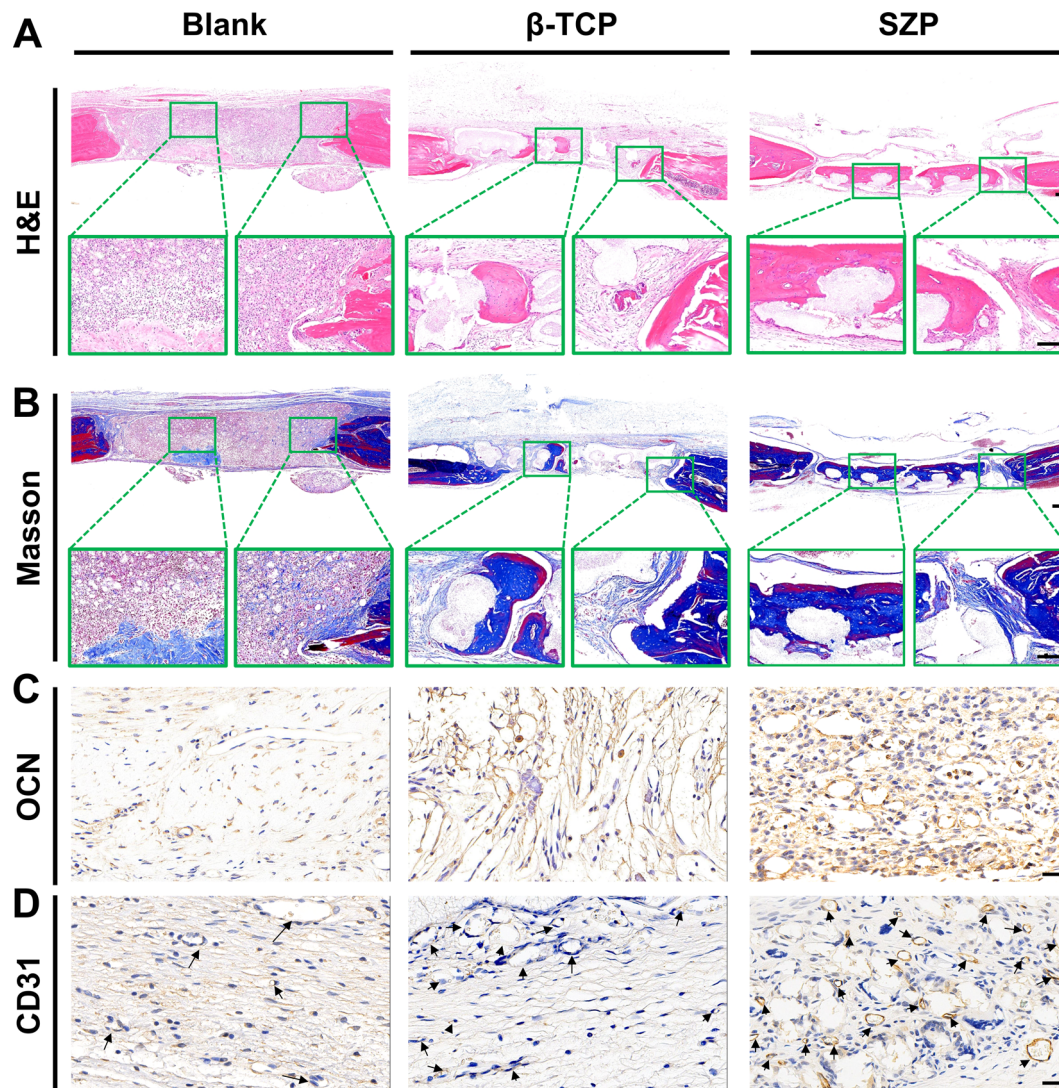
This journal is © The Royal Society of Chemistry 2023

J. Mater. Chem. B, 2023, **11**, 5469–5482 | **5479**

Fig. 10 Histological analysis of the newly formed bone tissues in the defects. Representative H&E staining (A) and Masson's trichrome staining (B) of the craniums with cranial defects after implantation of 3D printed SZP and β-TCP scaffolds for 4 weeks. Scale bar: 200 μm. Representative immuno-histochemistry staining of osteogenic marker OCN (C) and angiogenic marker CD31 (D) in newly formed tissues. Scale bar: 20 μm.

mixed with β-TCP for 3D printed scaffolds which enhance osteogenesis *via* the activation of the p38 signaling pathway.[36] This study further indicates that Zn^{2+} probably promotes osteogenesis through p38 signaling modulation. Another study has found enhanced cell adhesion, proliferation, and cytocompatibility of β-TCP after induction of Sr^{2+}.[37] All these studies demonstrate the promotive function of Zn^{2+} and Sr^{2+} in bone formation. Thus, single-phased SZP scaffolds are promising for promoting osteogenesis *via* direct modulation of bone cells in bone regeneration.

Beyond osteogenesis, angiogenesis is also crucial for the viability of bone scaffolds.[38] Blood vessels inside the bone play a crucial role in bone remodeling and regeneration *via* providing bone precursor cells. Compared to β-TCP scaffolds, SZP scaffolds were found to lead to promoted proliferation, migration and tube formation of HUVECs, as well as mRNA expression of angiogenic factors bFGF, eNOS and HIF-1α (Fig. 4).

This can be probably ascribed to Sr released from SZP scaffolds, by which vascular formation is facilitated,[39] together with upregulated angiogenic gene expression and increased tube formation by HUVECs.[40] Other than Sr, other elements such as copper, cobalt and silicon have also been widely reported as pro-angiogenic factors.[41] More interestingly, the combination of these elements may generate a synergistic effect on angiogenesis and further enhance the repair of the bone defect.[9,40] Hence, the SZP scaffolds we proposed are potent bone grafts as a result of their great angiogenic enhancement.

In addition to the direct effect, macrophage-modulated osteoimmunomodulation also plays a pivotal role in bone grafting.[42–44] To unveil this, SZP or β-TCP conditioned medium was collected from macrophages after co-culturing with SZP or β-TCP scaffolds for the assessment of macrophage-mediated immunomodulation, respectively. SZP-conditioned medium induced higher proliferation of osteoblasts than the β-TCP

5480 | *J. Mater. Chem. B*, 2023, **11**, 5469–5482

This journal is © The Royal Society of Chemistry 2023

conditioned medium (Fig. 6), which can be explained by a decrease of Fas-mediated apoptosis of osteoblasts *via* down-regulation of IL-1β and TNF-α.[45] On the other hand, upregulated anti-inflammatory factor TGF-1β can strongly enhance osteoblast differentiation through BMP-2 signaling.[46] These could probably result from Zn released from SZP scaffolds.[11] A similar phenomenon has been observed in Liu's study as Zn homeostasis is essential in periodontal regeneration as a result of its capability to defend immune response and elevate the proliferation and differentiation of local cells.[47] Furthermore, the decreased mRNA expression of M1 macrophage marker iNOS and upregulated mRNA expression of M2 macrophage marker CD206 (Fig. 5) indicate that SZP scaffolds can induce macrophage polarization toward the M2 phenotype, which is confirmed by a previous study.[29] This may be attributed to Zn^{2+} released from SZP scaffolds which is able to induce M2 polarization of macrophages *via* the PI3K/Akt/mTOR pathway.[14] Generally, activated macrophages are classified into M1 and M2 phenotypes for inflammatory response and tissue remodeling, respectively.[48] Timely switch from M1 to M2 macrophages is pivotal in bone tissue engineering, and the extension of the M1 phase brings about fibrous encapsulation and ceases new bone formation.[49] M2 macrophages are conducive to angiogenesis and osteogenesis *via* promoting tube formation capacity and osteogenic capacity, respectively.[50] Thus, the proposed SZP scaffolds in this study are promising for bone grafting due to excellent macrophage-mediated angiogenesis and osteogenesis.

In addition, bone graft-related infections usually lead to treatment failure, which limits bone defect repair and even increases the mortality rate.[51] Therefore, scaffolds with anti-bacterial effects are more promising for bone grafting. A number of strategies have been conducted to eliminate bone graft-related infections, among which the incorporation of metal ions such as Zn^{2+} and Cu^{2+} are widely utilized due to their ability to inactive bacteria *via* damaging the cells and increasing local pH.[12,41,52] Consistently, our study also observed that SZP scaffolds significantly reduced bacterial viability of *S. aureus* and *E. coli*, revealing excellent anti-bacterial effects of SZP materials. Similarly, utilizing the anti-bacterial function of silver ions (Ag^+), β-TCP has been bestowed anti-bacterial activity by the Ag dopant, and the anti-bacterial activity has been significantly improved by Zn/Ag co-dopant.[53] This phenomenon can be probably ascribed to the synergistic effect of Ag^+ and Zn^{2+}, or the particle size of the materials. Zn/Ag co-dopant has led to a smaller particle size of the materials than the Ag dopant,[53] suggesting a larger surface area to volume ratio and a faster ion release. As a consequence, more ions are accumulated for anti-bacterial activity. Though the Ag-doped materials present better anti-bacterial properties than the proposed SZP materials in this study, Ag-doped materials have limited applications due to their high toxicity. Thus, SZP is a promising anti-bacterial biomaterial with high biocompatibility for clinical application including repairing bone defect by reducing implant-related infections.

There are also some limitations in this study. For example, the mechanical properties and porous structure of the proposed 3D-printed SZP scaffolds are only comparable to cancellous bone, rather than compact bone. The *in vitro* degradation study could only partially mimic the degradation process of the scaffolds in the human body. The underlying mechanisms of the bioactive ions as well as their interactions are still unclear. Therefore, more elaborate experiments are needed in further study to solve the above issues.

5. Conclusions

In summary, 3D-printed SZP scaffolds were proven to promote bone regeneration both in a direct and an indirect manner. The proposed SZP scaffolds in this study exhibit multifunctional properties including: (1) equivalent mechanical properties and improved solubility; (2) enhanced anti-bacterial effect; (3) direct stimulation of osteogenesis and angiogenesis and (4) osteo-immunomodulation *via* M2 macrophages compared to traditionally used β-TCP scaffolds.

Conflicts of interest

There are no conflicts to declare.

Acknowledgements

References

1 K. J. Burg, S. Porter and J. F. Kellam, *Biomaterials*, 2000, **21**, 2347–2359.

2 J. Giron, E. Kerstner, T. Medeiros, L. Oliveira, G. M. Machado, C. F. Malfatti and P. Pranke, *Braz. J. Med. Biol. Res.*, 2021, **54**, e11055.

3 H. Wei, J. Cui, K. Lin, J. Xie and X. Wang, *Bone Res.*, 2022, **10**, 1–19.

4 X. Yu, X. Wang, D. Li, R. Sheng, Y. Qian, R. Zhu, X. Wang and K. Lin, *Chem. Eng. J.*, 2022, **433**, 132799.

5 J. Cui, X. Yu, B. Yu, X. Yang, Z. Fu, J. Wan, M. Zhu, X. Wang and K. Lin, *Adv. Healthcare Mater.*, 2022, **11**, e2200571.

6 C. Yang, Z. Zheng, M. R. Younis, C. Dong, Y. Chen, S. Lei, D. Y. Zhang, J. Wu, X. Wu, J. Lin, X. Wang and P. Huang, *Adv. Funct. Mater.*, 2021, **31**, 2101372.

This journal is © The Royal Society of Chemistry 2023

J. Mater. Chem. B, 2023, **11**, 5469–5482 | **5481**

7 C. Yang, H. Ma, Z. Wang, M. R. Younis, C. Liu, C. Wu, Y. Luo and P. Huang, *Adv. Sci.*, 2021, **8**, e2100894.

8 M. Xing, Y. Jiang, W. Bi, L. Gao, Y. L. Zhou, S. L. Rao, L. L. Ma, Z. W. Zhang, H. T. Yang and J. Chang, *Sci. Adv.*, 2021, **7**, eabe0726.

9 L. Mao, L. Xia, J. Chang, J. Liu, L. Jiang, C. Wu and B. Fang, *Acta Biomater.*, 2017, **61**, 217–232.

10 B. Wan, R. Wang, Y. Sun, J. Cao, H. Wang, J. Guo and D. Chen, *Front. Bioeng. Biotechnol.*, 2020, **8**, 591467.

11 W. Liu, J. Li, M. Cheng, Q. Wang, K. W. K. Yeung, P. K. Chu and X. Zhang, *Adv. Sci.*, 2018, **5**, 1800749.

12 I. Cacciotti, *J. Mater. Sci.*, 2017, **52**, 8812–8831.

13 P. Kazimierczak, J. Golus, J. Kolmas, M. Wojcik, D. Kolodynska and A. Przekora, *Biomater. Adv.*, 2022, **139**, 213011.

14 X. Huang, D. Huang, T. Zhu, X. Yu, K. Xu, H. Li, H. Qu, Z. Zhou, K. Cheng, W. Wen and Z. Ye, *J. Nanobiotechnol.*, 2021, **19**, 1–20.

15 B. M. Hidalgo-Robatto, M. López-Álvarez, A. S. Azevedo, J. Dorado, J. Serra, N. F. Azevedo and P. González, *Surf. Coat. Technol.*, 2018, **333**, 168–177.

16 R. Cruz, J. Calasans-Maia, S. Sartoretto, V. Moraschini, A. M. Rossi, R. S. Louro, J. M. Granjeiro and M. D. Calasans-Maia, *Ceram. Int.*, 2018, **44**, 1240–1249.

17 K. Zuo, L. Wang, Z. Wang, Y. Yin, C. Du, B. Liu, L. Sun, X. Li, G. Xiao and Y. Lu, *ACS Appl. Mater. Interfaces*, 2022, **14**, 7690–7705.

18 Z. Zhong, X. Wu, Y. Wang, M. Li, Y. Li, X. Liu, X. Zhang, Z. Lan, J. Wang, Y. Du and S. Zhang, *Bioact. Mater.*, 2022, **10**, 195–206.

19 M. Hassan, M. Sulaiman, P. D. Yuvaraju, E. Galiwango, I. U. Rehman, A. H. Al-Marzouqi, A. Khaleel and S. Mohsin, *J. Funct. Biomater.*, 2022, **13**, 13.

20 V. Khidhirbrahmendra, S. J. Basha, M. Avinash, U. S. U. Thampy, C. V. Reddy and R. V. S. S. N. Ravikumar, *J. Mater. Sci.: Mater. Electron.*, 2019, **30**, 5120–5129.

21 L. Chen, C. Deng, J. Li, Q. Yao, J. Chang, L. Wang and C. Wu, *Biomaterials*, 2019, **196**, 138–150.

22 C. Yang, X. Wang, B. Ma, H. Zhu, Z. Huan, N. Ma, C. Wu and J. Chang, *ACS Appl. Mater. Interfaces*, 2017, **9**, 5757–5767.

23 K. J. Livak and T. D. Schmittgen, *Methods*, 2001, **25**, 402–408.

24 C. C. Liang, A. Y. Park and J. L. Guan, *Nat. Protoc.*, 2007, **2**, 329–333.

25 C. Yang, Z. Huan, X. Wang, C. Wu and J. Chang, *ACS Biomater. Sci. Eng.*, 2018, **4**, 608–616.

26 L. Zhang, G. Yang, B. N. Johnson and X. Jia, *Acta Biomater.*, 2019, **84**, 16–33.

27 D. Bicho, R. F. Canadas, C. Goncalves, S. Pina, R. L. Reis and J. M. Oliveira, *J. Biomater. Sci., Polym. Ed.*, 2021, **32**, 1966–1982.

28 X. Li, Q. Zou, J. Wei and W. Li, *Composites, Part B*, 2021, **222**, 109084.

29 D.-W. Zhao, C. Liu, K.-Q. Zuo, P. Su, L.-B. Li, G.-Y. Xiao and L. Cheng, *Chem. Eng. J.*, 2021, **408**, 127362.

30 H. Ma, C. Yang, Z. Ma, X. Wei, M. R. Younis, H. Wang, W. Li, Z. Wang, W. Wang, Y. Luo, P. Huang and J. Wang, *Adv. Healthcare Mater.*, 2022, **11**, 2102837.

31 C. Yang, X. Gao, M. R. Younis, N. T. Blum, S. Lei, D. Zhang, Y. Luo, P. Huang and J. Lin, *Chem. Eng. J.*, 2021, **408**, 127959.

32 M. Bohner, B. L. G. Santoni and N. Dobelin, *Acta Biomater.*, 2020, **113**, 23–41.

33 Z. Xu, J. Long, N. Zhang, H. Cao, W. Tang, K. Shi, X. Wang, S. Moya, L. Duan, H. Pan, Y. Lai, D. Wang and G. Wang, *Colloids Surf., B*, 2019, **176**, 420–430.

34 D. K. J. Patrick O'Connor, M. Teitelbaum, S. S. Lin and J. A. Cottrell, *Materials*, 2020, **13**, 2211.

35 I. Ullah, M. A. Siddiqui, H. Liu, S. K. Kolawole, J. Zhang, S. Zhang, L. Ren and K. Yang, *ACS Biomater. Sci. Eng.*, 2020, **6**, 1355–1366.

36 X. Yuan, T. Lu, F. He, T. Wu, X. Wang and J. Ye, *J. Mater. Chem. B*, 2022, **10**, 9639–9653.

37 I. V. Fadeeva, D. V. Deyneko, A. A. Forysenkova, V. A. Morozov, S. A. Akhmedova, V. A. Kirsanova, I. K. Sviridova, N. S. Sergeeva, S. A. Rodionov, I. L. Udyanskaya, I. V. Antoniac and J. V. Rau, *Molecules*, 2022, **27**, 6085.

38 I. L. Tsiklin, A. V. Shabunin, A. V. Kolsanov and L. T. Volova, *Polymers*, 2022, **14**, 3222.

39 S. Zhang, Y. Dong, M. Chen, Y. Xu, J. Ping, W. Chen and W. Liang, *J. Artif. Organs*, 2020, **23**, 191–202.

40 S. Kargozar, N. Lotfibakhshaiesh, J. Ai, M. Mozafari, P. Brouki Milan, S. Hamzehlou, M. Barati, F. Baino, R. G. Hill and M. T. Joghataei, *Acta Biomater.*, 2017, **58**, 502–514.

41 C. Fan, Q. Xu, R. Hao, C. Wang, Y. Que, Y. Chen, C. Yang and J. Chang, *Biomaterials*, 2022, **287**, 121652.

42 Y. Liu, B. Zhang, F. Liu, Y. Qiu, W. Mu, L. Chen, C. Ma, T. Ye and Y. Wang, *Eng. Regener.*, 2022, **3**, 339–351.

43 X. Zhang, J. Cui, L. Cheng and K. Lin, *J. Mater. Chem. B*, 2021, **9**, 3489–3501.

44 W.-W. Yu, Q.-Q. Wan, Y. Wei, Y.-T. Li, Q.-H. Li, T. Ye, K.-H. Xu, J.-H. Song, C. Lei, M.-C. Wan, K. Jiao, F. R. Tay and L.-N. Niu, *Eng. Regener.*, 2022, **3**, 270–282.

45 M. Tsuboi, A. Kawakami, T. Nakashima, N. Matsuoka, S. Urayama, Y. Kawabe, K. Fujiyama, T. Kiriyama, T. Aoyagi, K. Maeda and K. Eguchi, *J. Lab. Clin. Med.*, 1999, **134**, 222–231.

46 G. Chen, C. Deng and Y. P. Li, *Int. J. Biol. Sci.*, 2012, **8**, 272–288.

47 Y. Liu, X. Li, S. Liu, J. Du, J. Xu, Y. Liu and L. Guo, *Oral Dis.*, 2022, **0**, 1–15.

48 T. Buchacher, A. Ohradanova-Repic, H. Stockinger, M. B. Fischer and V. Weber, *PLoS One*, 2015, **10**, e0143593.

49 Z. Chen, J. Yuen, R. Crawford, J. Chang, C. Wu and Y. Xiao, *Biomaterials*, 2015, **61**, 126–138.

50 C. Yang, C. Zhao, X. Wang, M. Shi, Y. Zhu, L. Jing, C. Wu and J. Chang, *Nanoscale*, 2019, **11**, 17699–17708.

51 E. D. Rennert-May, J. Conly, S. Smith, S. Puloski, E. Henderson, F. Au and B. Manns, *Infect. Control Hosp. Epidemiol.*, 2018, **39**, 1183–1188.

52 Q. Xu, F. Jiang, G. Guo, E. Wang, M. R. Younis, Z. Zhang, F. Zhang, Z. Huan, C. Fan, C. Yang, H. Shen and J. Chang, *Nano Today*, 2021, **41**, 101330.

53 Y.-J. Chou, H. S. Ningsih and S.-J. Shih, *Ceram. Int.*, 2020, **46**, 16708–16715.

5482 | *J. Mater. Chem. B*, 2023, **11**, 5469–5482

This journal is © The Royal Society of Chemistry 2023